Icarus xxx (2015) xxx–xxx

Contents lists available at ScienceDirect

Icarus

journal homepage: www.journals.elsevier.com/icarus

Visible and Near-Infrared (VNIR) reflectance spectroscopy of glassy igneous material: Spectral variation, retrieving optical constants and particle sizes by Hapke model

C. Carli [a,*], T.L. Roush [b], G. Pedrazzi [c], F. Capaccioni [a]

[a] IAPS-INAF, Roma, Italy
[b] AMES Research Center-NASA, CA, USA
[c] Biophysics and Medical Physics Unit, Department of Neuroscience, University of Parma, Italy

ARTICLE INFO

Article history:
Received 3 July 2015
Revised 15 October 2015
Accepted 29 October 2015
Available online xxxx

Keywords:
Mineralogy
Regoliths
Spectroscopy

ABSTRACT

Silicate glasses with igneous compositions can be an important constituent of planetary surface material via effusive volcanism or impact cratering processes. Different planetary surfaces are mapped with hyper-spectrometers in the VNIR, and in this spectral range crystal field absorptions are useful in discriminating iron bearing silicate components. For these reasons studying glassy materials, and their optical constants, is an important effort to better document and understand spectral features of Solar System silicate crusts where glasses are present, but may be difficult to map. In our work we present a set of four different synthetic glasses, produced under terrestrial conditions, with variable composition and in particular an increasing amount of iron. The VNIR spectra show, for all the compositions, two absorptions are present near 1.1 and 1.9 μm but reflectance, slope and absorption shape varies with composition. We measured the reflectance of different particle sizes of the samples and used radiative transfer models to estimate the optical constants as a function of wavelength. We used the retrieved optical constants to estimate the particle size from the measured reflectances and the results fall within the known sieve range. We qualitatively discuss the effect of the shape and distribution of particles on the application of the model.

1. Introduction

One of the principal products of extrusive volcanism and impact cratering is glassy material, which can be an abundant component and significantly influence the VNIR reflectance spectral signature of a surface region. The spectral information of those regions will be not only characterized by the crystalline silicate absorption features but by any presence of the glass (e.g. Carli and Sgavetti, 2011; Carli et al., 2015; for examples relate to effusive rocks case).

Different type of glasses have been proposed and identified, in particular on the lunar surface, where the returned samples permitted a detailed analysis. The wide compositional variations of effusive products and of the different terrains affected by impact processes result in glassy materials having a wide range of compositions. Moreover the different environmental conditions present on the different bodies can result in important variation in the glasses. Previous research has shown that different FeO/TiO_2 ratio and/or change in oxygen fugacity can affect the spectral information at VNIR wavelengths. In this spectral range the glasses are generally characterized by two crystal field (CF) absorptions near 1 and 2 μm attributed to Fe^{2+} absorptions (e.g. Adams and McCord, 1971; Dyar and Burns, 1981; Burns, 1993; Tompkins and Pieters, 2010) and variable reflectance levels and slope.

Lunar glasses are generally the most characterized type of glasses in the VNIR (0.4–2.5 μm) range. They are described as material with different colors, e.g. brown, red, orange, yellow, green, and, generally, they correspond to glasses with high iron content and variable amounts of titanium (Dyar and Burns, 1981; Gillis-Davis et al., 2007, 2008). This variation in compositions is manifested spectrally as a change of reflectance and slope, particularly in the visible, whereas the spectra in the near-IR always exhibit absorption bands near 1 and 2 μm (e.g. Tompkins and Pieters, 2010). In some studies of lunar glass analogs focusing on high Fe and Ti concentrations, different abundances of dark glasses, relative to the crystalline silicates, were shown to reduce the intensity of silicate absorption bands (e.g., Adams and McCord, 1971; Cloutis et al., 1990; Tompkins and Pieters, 2010).

* Corresponding author.
E-mail address: cristian.carli@iaps.inaf.it (C. Carli).

http://dx.doi.org/10.1016/j.icarus.2015.10.032
0019-1035/

Glasses with different compositions, composed with different abundance of other major elements (e.g. Cr, Al, Mg, Ca, Na) were not extensively explored using VNIR spectroscopy, or only marginally, as typical olivine or pyroxene stoichiometric composition glasses (Jager et al., 1994; Dorschner et al., 1995). A few other studies explored the influence of different oxygen fugacity during melting (i.e. Bell et al., 1976) but did not measure the reflectance of the materials as would be obtained from remote sensing observations.

In fact, Bell et al. (1976) measured the VNIR transmission, and determined the absorption coefficients of several synthetic glasses produced using different oxygen fugacity with a composition similar to an Fe–Ti basalt by varying the amount of FeO and TiO_2 from iron-free to titanium-free end-members. This study, developed to determine oxygen fugacity, iron and titanium content both in lunar samples and on Moon's surface, showed that, at ambient terrestrial conditions, the spectrum of Ti-free sample show a strong shoulder in the VNIR caused by Fe^{3+} charge transfer transition towards the ultraviolet. Fe^{3+} is also probably responsible for a weak 0.545 μm absorption (i.e. spin forbidden), whereas the Fe-free glass shows no Ti^{4+} absorption in this region. With decreasing $P(O_2)$, the Fe^{3+} disappears as well as its absorption, but titanium became Ti^{3+} with the appearance of an absorption at 0.5 μm. At this lower oxygen fugacity the 1 and 2 μm bands are always present (Bell et al., 1976).

Attempting to understand the composition of three lunar pyroclastic deposits Wilcox et al. (2006) described a way to calculate the optical constant of glassy material and how to apply the radiative transfer modeling (e.g. Hapke, 1981, 2001; Hapke et al., 1993). They consider absorption coefficients of synthetic glasses measured by Bell et al. (1976), converting the absorption coefficient (α) in the imaginary refractive index, k, with the following relationship $\alpha = 4\pi k/\lambda$, and they determined the real part, n, using the equation of Church and Johnson (1980) that relates n to the chemical composition. Wilcox et al. (2006) evaluated how the k-value was related to $FeO + x * TiO_2$. They validate the methods fitting an Apollo15 green glass, allowing the particle size and submicroscopic metallic iron amount (SMFe) to vary in order to determine the best match with the known iron and titanium composition. They found that the model fit the spectra quite well for wavelengths >0.7 μm. For shorter wavelengths the model yields a darker spectrum than what was measured. The best fit was found with a grain size of 18.7 μm, close to the normalized size frequency distribution, and no SMFe, compatible with the immaturity of the sample. Then they fit the lunar spectra of the three regions and infer a specific composition for each region. They found a good fit with glassy materials rather than the presence of black beads (dark devitrified material in pyroclastic deposits), except for one region where the fit with a mixture of glass and black beads give a value only marginally worse. They suggest that further measurements of optical constants and their variation with composition would be useful in, particular for the short wavelength range.

Here, we present a study of VNIR bidirectional reflectance spectra of synthetic glasses produced from four basic rock compositions. The chosen compositions extend from relative low to high iron contents (i.e., from high plagioclase, anorthositic, to high mafic, basaltic, glasses compositions). In an effort to extend the laboratory measurements to other grain sizes, or even mixtures, we estimated the complex refractive indices, commonly referred to as optical constants, of the glass samples using radiative transfer models. In Section 2 we describe our methodology in preparation and characterization of the samples. In Section 3 we present the approach used to estimate the average complex refractive indices of each glass and use these to assess how well the known particle size can be estimated using these values. We follow with a discussion of the results in Section 4 and provide a summary in Section 5.

2. Methods

2.1. Sample preparation

Four different rock samples were used to produce glasses (Table 1): an anorthosite, two gabbronorites (Carli et al., 2014b) and an hawaiitic basalt (Pasquarè et al., 2008). The sample choice was principally driven by: (a) basic igneous material, having compositions which, in theory, could be genetically related; (b) variability of iron content; and (c) low amount of secondary alteration. The rock samples were cut and ground, producing a thin section representative of the original rocks for optical and mineral chemistry analyses and coarse powder material to be melted. A portion of the coarse powder was ground to finer sizes for chemical analysis of the rocks as a comparison with the glasses composition.

The rest of the coarse powders were melted in a high temperature furnace (Nabertherm HT17/16) at 1500 °C for an hour and then quenched in air. The furnace operates at oxidizing terrestrial conditions. Glasses were then ground and reduced to powder for chemical analysis and for spectral measurements. The ⩽250 μm sieve fraction was subsequently ground and dry sieved, by repeatedly shaking, into several particle size separates of 250–224, 224–200, 200–180, 180–150, 150–125, 125–100, 100–75, 75–50, and 50–20 μm.

2.2. Sample analysis

2.2.1. Rock and glass compositions

Preliminary evaluation by optical microscope revealed that the rock samples have a low amount of hydrate alteration, resulting in a low amount of loss during melting. We also confirmed the homogeneity of the glasses and absence of inclusions. Chemical analysis of samples performed to document the bulk rock composition via X-ray fluorescence (XRF) measurements on both rock and glass samples (Table 1). It is evident that bulk rock composition is unchanged after the melting.

Mossbauer analyses were performed to evaluate the oxidation state of the iron in the glasses. Transmission Fe Mössbauer spectra were obtained on a few milligrams of powdered sample at room temperature using a Co–57(Rh) thin source. The spectrometer operated in constant acceleration mode with a symmetric velocity ranging between ±4 mm/s. The velocity was calibrated against a standard α-Fe. Fitting of spectra has been performed using the software Recoil (Lagarec and Rancourt, 1998), using doublets of Lorentzian line shape. Refined parameters for each sample are given in Table 2. The Mössbauer spectra of all glasses are shown in Fig. 1a. It is clear that three samples have the same absorptions, with variable intensity related to the total iron content, only St18g, the most Fe-poor, shows a slightly different spectrum with less prominent absorption at ≈1 mm/s. Fig. 1b shows an example of how the principal peaks are fitted using two Lorentzian doublets: the one with largest QS can be assigned to Fe^{2+}, while the other band is indicative of Fe^{3+}.

2.2.2. Density

We measured the density of our samples both for rocks and glasses using an industrial gas pycnometer (Ultraphyc1200Q, Quantachrome®) weighing a representative piece of bulk sample and then purging the chamber of the pycnometer with a gas (He). The results are summarized in Table 3 where it is clear that glass samples, despite analogous bulk rock composition (Table 1), have lower density values. Similar behavior was seen also by Karamanov and Pelino (1999) and Fowle (1921) for different silicate glasses. This density difference increases linearly with the iron content in samples.

Please cite this article in press as: Carli, C., et al. Visible and Near-Infrared (VNIR) reflectance spectroscopy of glassy igneous material: Spectral variation, retrieving optical constants and particle sizes by Hapke model. Icarus (2015), http://dx.doi.org/10.1016/j.icarus.2015.10.032

Table 1
XRF analysis of major elements of rocks and synthetic glasses. Fe_2O_{3tot} = FeO + Fe_2O_3. *L.O.I* = loss on ignition.

	Ol-basalt PY7MM	Gabbronorite ST8	Gabbronorite ST14	Anorthosite ST18	PY7MMg	ST8g	ST14g	ST18g
SiO_2	48.67	51.10	50.41	48.70	47.68	50.96	49.53	48.18
TiO_2	1.91	0.15	0.14	0.09	1.88	0.15	0.14	0.08
Al_2O_3	16.36	16.83	21.07	29.44	16.10	16.34	20.72	29.36
Fe_2O_{3tot}	11.30	7.06	4.45	1.79	11.28	7.19	4.46	1.78
MnO	0.17	0.13	0.09	0.03	0.17	0.14	0.09	0.03
MgO	7.15	12.40	7.71	2.05	7.05	12.84	7.61	1.92
CaO	9.16	10.70	15.46	15.92	9.06	10.96	15.32	15.85
Na_2O	3.65	1.11	1.48	2.25	3.56	1.14	1.46	2.24
K_2O	1.33	0.08	0.13	0.08	1.30	0.08	0.12	0.08
P_2O_5	0.45	0.01	0.01	0.01	0.45	0.01	0.01	0.01
Tot	100.15	99.57	100.95	100.36	98.53	99.81	99.46	99.53
L.O.I.	0.73	1.23	0.92	1.60	0.30	0.28	0.26	0.23

Table 2
Mössbauer parameters for Fe, Mg end-member. IS = isomeric shift; QS = quadrupole splitting; FWHM = full width at half maximum. χ^2 = reduced chi-square.

Sample	Assignment	IS (mm/s)	QS (mm/s)	FWHM (mm/s)	Area (%)	χ^2
St18g	Fe^{2+}	1.023	1.914	0.641	49.2	1.333
	Fe^{3+}	0.305	1.323	0.785	50.8	
St14g	Fe^{2+}	1.047	1.918	0.562	40.5	1.347
	Fe^{3+}	0.313	1.313	0.668	59.5	
St8g	Fe^{2+}	1.042	1.913	0.572	38.7	1.421
	Fe^{3+}	0.304	1.304	0.601	61.3	
Py7MMg	Fe^{2+}	1.050	1.916	0.570	40.0	1.829
	Fe^{3+}	0.304	1.248	0.546	60.0	

2.2.3. Real part (*n*) of the refractive indexes

The real part of the refractive index was calculated measuring the Brewster angle (θ_B), where θ_B = arctg ($n2/n1$), where the two media are the glass ($n2$) and the air ($n1$). We assumed that the imaginary index for silicate material is ~ five orders of magnitude smaller in the VNIR, so the real part can be, to first order, considered equal to $n2$ and constant in the VNIR. The calculated values are shown in the last column of Table 3.

2.2.4. Reflectance

We measured bidirectional reflectance spectra from 0.35 to 2.5 μm at ambient conditions with a Field-Pro Spectrometer mounted on a goniometer. The spectra were acquired with 3 nm of spectral resolution in the visible and 10–12 nm in the near-infrared. These are resampled by the spectrometer software to a spacing of 1 nm. Reflectance measurements were obtained with incident (*i*) and emission (*e*) angles of 30° and 0°, respectively. A light source was a QTH (quartz–tungsten–halogen) lamp producing an illuminated spot of ≈0.5 cm^2. The calibration of the spectrometer was performed with a 99% reflectance Spectralon (Labsphere®) and the spectra were corrected for the Spectralon reflectance.

2.2.5. Particle size and shape

We determined the particle size and shape variation of the 50–20 and 250–224 μm size separates, by SEM imaging. Carbon tape with adhesive on both sides was place on a SEM sample stage and then particles of each sample were sprinkled onto the exposed tape. The sample stage was placed into a Hitachi model 4000 SEM operating at 15 kV and images were typically obtained at magnifications of approximately 50, 100, 250, 500, 1000, and 2000. Fig. 2 illustrates the typical nested sequence.

The original images were edited in Photoshop® to remove artifacts attributable to the carbon tape, eliminate grains not completely present in the image, and eliminate duplication of counting grains in a nested sequence. We used ImageJ (Abramoff et al., 2004; Schneider et al., 2012; Rasband, 2014) to determine particle sizes from the edited SEM images. A threshold was determined for each image to isolate grains from the background. An example is shown in Fig. 3. Particle size information was extracted from each image using the ImageJ *analyze particles* function. The

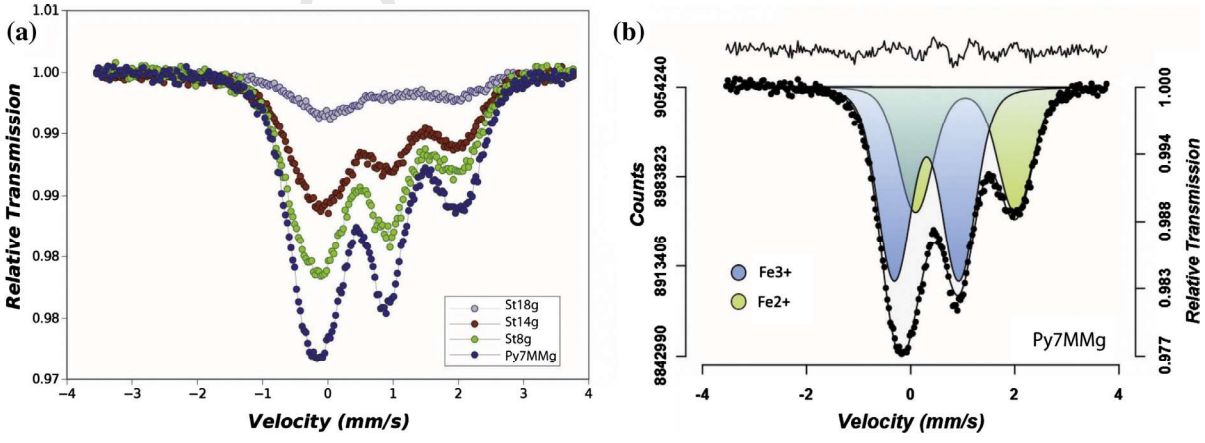

Fig. 1. (a) Room temperature Mössbauer spectra for the four glasses. The spectra show clearly the presence of both Fe^{2+} and Fe^{3+}. (B) Example of fitting components for Py7MMg sample, in blue the doublet representing the Fe^{3+}, in green the one representing the Fe^{2+}. (For interpretation of the references to color in this figure legend, the reader is referred to the web version of this article.)

Please cite this article in press as: Carli, C., et al. Visible and Near-Infrared (VNIR) reflectance spectroscopy of glassy igneous material: Spectral variation, retrieving optical constants and particle sizes by Hapke model. Icarus (2015), http://dx.doi.org/10.1016/j.icarus.2015.10.032

Table 3
Density values of both rock and glass samples and refractive indexes obtained by measuring the Brewster angle (a red light, 635 nm, was used). This is the real index value (n) used as first approximation with Hapke model (see text for more details).

	Rock samples			Glass samples		n
	Density (g/cm^3)	St.dev. (±)		Density (g/cm^3)	St.dev. (±)	
St18	2.748	0.002	St18g	2.704	0.001	1.58
St14	2.914	0.005	St14g	2.736	0.001	1.60
St8	3.009	0.005	St8g	2.796	0.001	1.60
Py7	3.009	0.005	Py7g	2.790	0.005	1.62

results were displayed with an outline around each grain for confirmation. The properties recorded and subsequently used to determine the particle size variation include, for each grain, the grain number, area (square pixels), and the major and minor axes (pixels) of the fit ellipse. These values, along with the stated image length of the scale bar and the number of pixels comprising this length, are saved in an ASCII file.

The parameters from the image analyses were used to calculate the diameter of each grain via two pathways. The first used the recorded area (A) to determine the equivalent spherical particle diameter, d, via: $A = \pi r^2$, where the sphere radius, r, is $\frac{1}{2}d$. The second calculated the diameter from the elliptical area as, $A = \pi ab$, where a and b are the semi-major axes of the ellipse and are ½ the values recorded from the image analyses files. Thus, the equivalent spherical diameter is given by: $\pi r^2 = \pi ab$, yielding $r = (ab)^{1/2}$ and hence, $d = 2(ab)^{1/2}$. For the two representations we find that the resulting distributions are statistically indistinguishable for each particle size bin. So we only use the diameter of the equivalent spherical grain. The results for shape and size variations are discussed in Section 4.4.

3. Analytical approach

3.1. Retrieving the imaginary part of the refractive indices

Several papers in the last two decades have used the Hapke model (Hapke et al., 1993; Hapke, 2012) to determine the imaginary part (k) of the refractive index for minerals from reflectance spectra (e.g. Roush et al., 1990; Lucey, 1998; Roush et al., 2007; Warrel and Davidsson, 2010; Carli et al., 2014a). Here we provide a brief summary of this approach and an interested reader is referred to those papers and to Hapke et al. (1993) and Hapke (2012) for more details of the mathematical formalism. We initially assumed n to be constant at all wavelengths and equal to the measured value given in Table 3. Using this fixed value for n, k is calculated by minimizing the differences between the calculated and measured reflectance. Following Roush (2003, 2005) and Roush et al. (2007) we used a subtractive Kramers–Kroning (sKK) analysis to determine n as function of the wavelength. Using this wavelength dependent n, we return to the estimate a new k from the reflectance. We iterate between the reflectance model and sKK calculations until differences between subsequent values of n and k are essentially zero.

Assuming that the composition is not a function of particle size, we can better constrain the calculated refractive indices by determining the values for different particle sizes and averaging the different k-values. The particle size value used for each of the nine ranges is the average between the two sieves (e.g. for 250–224 μm we used 237 μm). Recently, Roush et al. (2014) showed that for a narrow size range the k-values retrieved using an average value is consistent with those retrieved by using a more

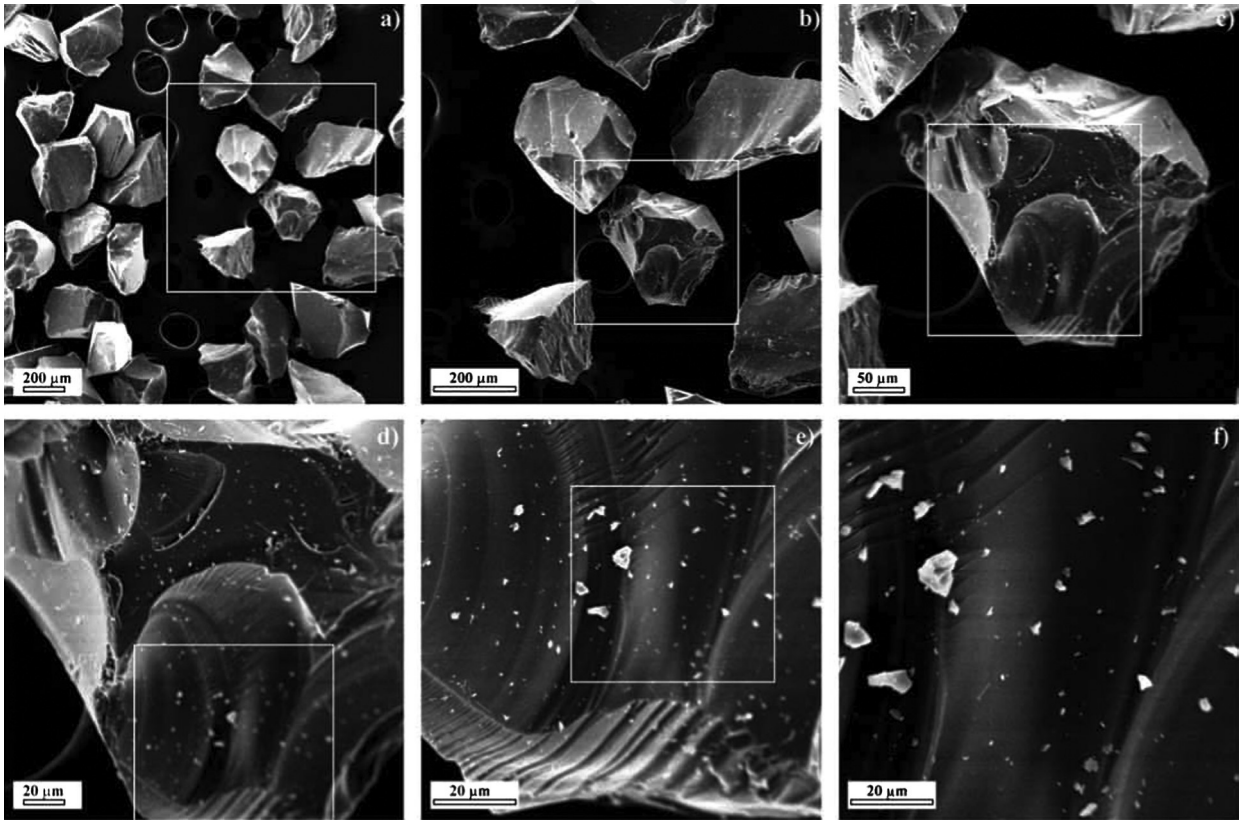

Fig. 2. SEM images of St18g samples, 250–224 μm, (a) ×100, box indicates where image b is located, (b) ×500, box indicates where image c is located, (c) ×1000, (d) ×2000, (e) ×2000, (f) ×2000. For these exact magnifications, a single pixel in the 512 × 512 image corresponds to 4, 2, 0.75, 0.33, 0.2, and 0.1 μm, respectively. However, magnifications were close to these values, with pixel scales determined by the scale bar on each image.

Please cite this article in press as: Carli, C., et al. Visible and Near-Infrared (VNIR) reflectance spectroscopy of glassy igneous material: Spectral variation, retrieving optical constants and particle sizes by Hapke model. Icarus (2015), http://dx.doi.org/10.1016/j.icarus.2015.10.032

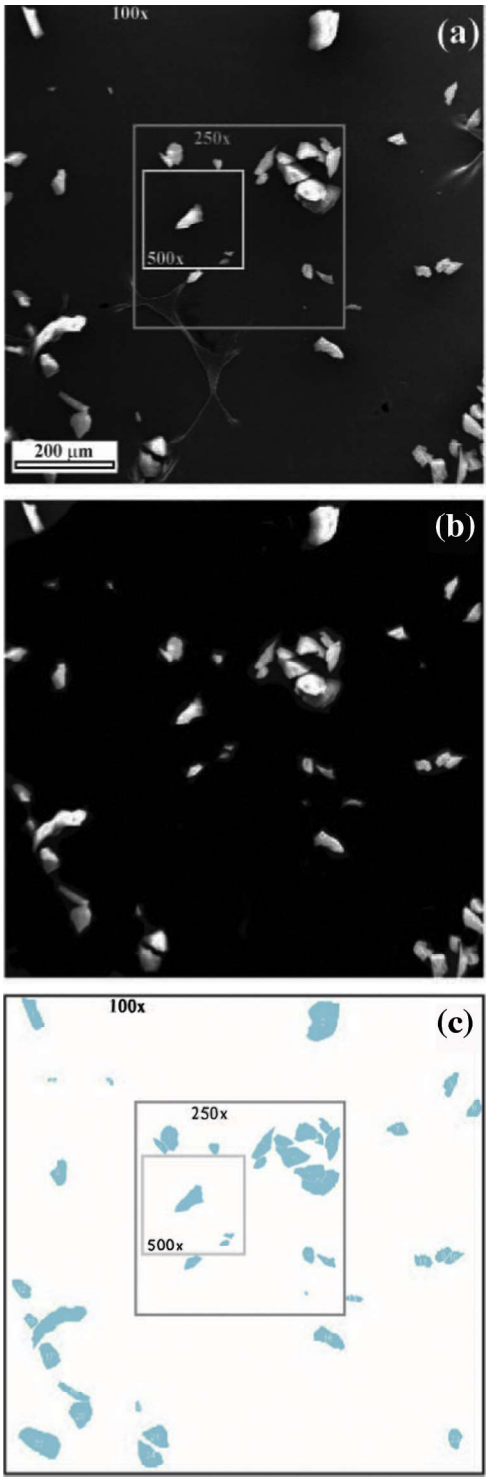

Fig. 3. SEM images of St18g samples, 50–20 μm. (a) Original image, artifacts due to the double-sided carbon tape are clearly recognizable. (b) Image a, after editing. (c) Image b, after applying a threshold and this image is used for particle size determination. Grains contained in the higher magnification images were eliminated from the lower magnification images.

complex areal or volumetric representations of the particle size distribution.

The assumptions considered here within the Hapke formalism (Hapke, 2012; and references therein) are discussed in Eqs. (1)–(6) of Roush (1994) and Eqs. (1)–(4) of Cruikshank et al. (1997). Briefly, here, we assumed isotropic scattering, the width of the opposition surge is assumed to be 0.05, because measurements were not obtained at multiple viewing geometries, and Hapke's internal scattering is set at 0, forcing the absorption coefficient to account for all the spectral behavior (see also Roush et al., 2007). Geometric conditions are known with $i = 30°$ and $e = 0°$. Similar to Warrel and Davidsson (2010) and Carli et al. (2014a) we do not account for porosity, introduced in Hapke (2008), in order to reduce the number of free parameters. Porosity can mainly influence the reflectance of samples, several laboratory studies (e.g. Kaasalainen, 2003; Näränen et al., 2004; Shepard and Helfenstein, 2011) have shown that compacted powders (low porosity) have in general greater reflectance than loose ones.

In summary the approach is:

1. Estimate k by applying the Hapke model to each spectrum using mean sieve particle sizes of 237, 212, 190, 165, 137.5, 112.5, 87.5, 62.5, and 35 μm, for the nine different size ranges, respectively. Assuming n, derived from the Brewster angle measurement, is constant over the entire wavelength region. After this initial calculation we have n_0(constant), $k_0(\lambda)$ for each size, of each sample.
2. Use the k_0 values in a sKK analysis to determine $n(\lambda)$.
3. Recalculate k using $n(\lambda)$ value, yielding $n_1(\lambda)$, $k_1(\lambda)$ both as function of wavelength.
4. Iteratively perform these calculations to get subsequent $n(\lambda)$'s via the sKK analysis, and then $k(\lambda)$'s via the Hapke model.

The resulting refractive indices are discussed in Section 4.3.

3.2. Fitting the particle sizes

Once the average final refractive indices were determined, they were used to investigate how well they describe the reflectance spectrum of each particle size separate. This involved fitting the laboratory spectrum using the derived refractive indices. The same mathematical model, used to determine the refractive indices, was used in a forward calculation. In this approach, all the parameters discussed for the model above were the same, except particle diameter which was the sole parameter permitted to vary during the iterative calculations. The best fit to the measured reflectance was determined using a χ^2-criterion. The downhill simplex method described in Press et al. (1992), specifically the amoeba routine, was used to search grain diameter parameter space, with only a single grain diameter to represent the particle size in the models. For each glass and sieve fraction, the model was investigated with an initial diameter estimate. These estimates were chosen to be as far as possible from the fitted size fraction (e.g. for 50–20 μm we used 250 μm, and vice versa we initially used 20 μm for the coarsest size). Each time a reflectance was calculated, the current grain diameter and χ^2-value was recorded. As illustrated in Fig. 4, this permits an evaluation of the parameter space explored during the fitting process. The sharpness of the χ^2 minimum defines how unique the solution is, and for the example in Fig. 4 the minimum is clearly $\leqslant \pm 5$ μm. The results for all samples, and comparison to the sieve size fractions, are discussed in Section 4.3 below.

4. Results

4.1. Reflectance spectra variation

As seen in Fig. 5, spectra of the synthetic glasses are characterized by absorptions near 1.1 and 1.9 μm commonly associated with Fe^{2+} absorptions (e.g. Adams and McCord, 1971; Dyar and Burns, 1981; Burns, 1993; Tompkins and Pieters, 2010). The four

Please cite this article in press as: Carli, C., et al. Visible and Near-Infrared (VNIR) reflectance spectroscopy of glassy igneous material: Spectral variation, retrieving optical constants and particle sizes by Hapke model. Icarus (2015), http://dx.doi.org/10.1016/j.icarus.2015.10.032

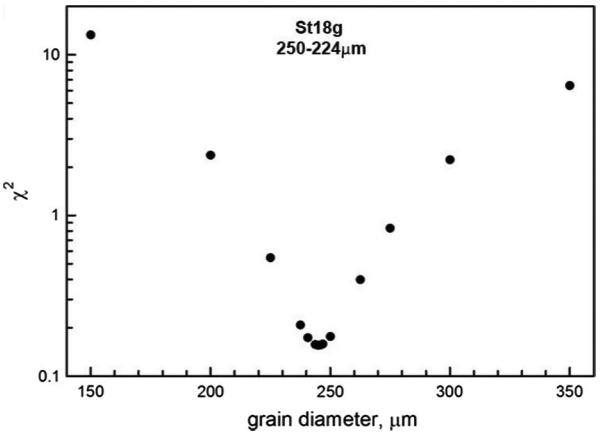

Fig. 4. Example of determination of the particle size using the derived refractive indices for sample St18g, the 250–224 μm sieve size fraction. The exhibits a clear χ^2 minimum at 245 ± 5 μm.

samples, despite the similarity (1.090 ± 0.005 μm and 1.908 ± 0.005 μm, excluding few outlier points) in band positions (band center), show spectra with different reflectance levels. The reflectance decreases with increasing iron content, whereas the slope in the infrared generally increases with increasing iron content. Each sample shows that both the spectral reflectance and slope vary with particle size (Fig. 5). Band position is almost unchanged with respect to the size variations (with a range from a ±4 nm to ±10 nm, from iron-poor St18g to iron-rich Py7MMg, for both 1.1 and 1.9 μm absorptions), whereas band intensity (band depth) varies with both composition and particle size (Fig. 6). Band depth is calculated as the difference between the continuum and the band center reflectance after the division with the continuum (Clark and Roush, 1984). The continuum is a linear segmented upper hull joining the reflectance maxima in the spectrum (Clark and Roush, 1984). Considering the four different compositions, the 1.1 μm band has low variability in depth for a fixed size, whereas the 1.9 μm band shows a stronger difference with composition; very weak for St18g and becoming deeper with increasing the total iron (see Fig. 6c). For all compositions both the band depths increase, almost linear, with the particle size, from 50–20 μm to 250–224 μm (see Fig. 6a and c). A few outliers are present, in particular for the band around 1.1 μm of the iron-rich Py7MMg. The trend of the depth for particle sizes bigger than 200–180 μm flattens and the positions are shifted to longer wavelength (towards 1.2 μm, see Fig. 6). This behavior could be explained with a band saturation effect due to the very low reflectance in the visible range (see Fig. 5).

4.2. Imaginary part of the refractive indices

We considered here the reflectance spectra from 0.4 to 2.4 μm to avoid the extremes of the wavelength range where QTH lamp

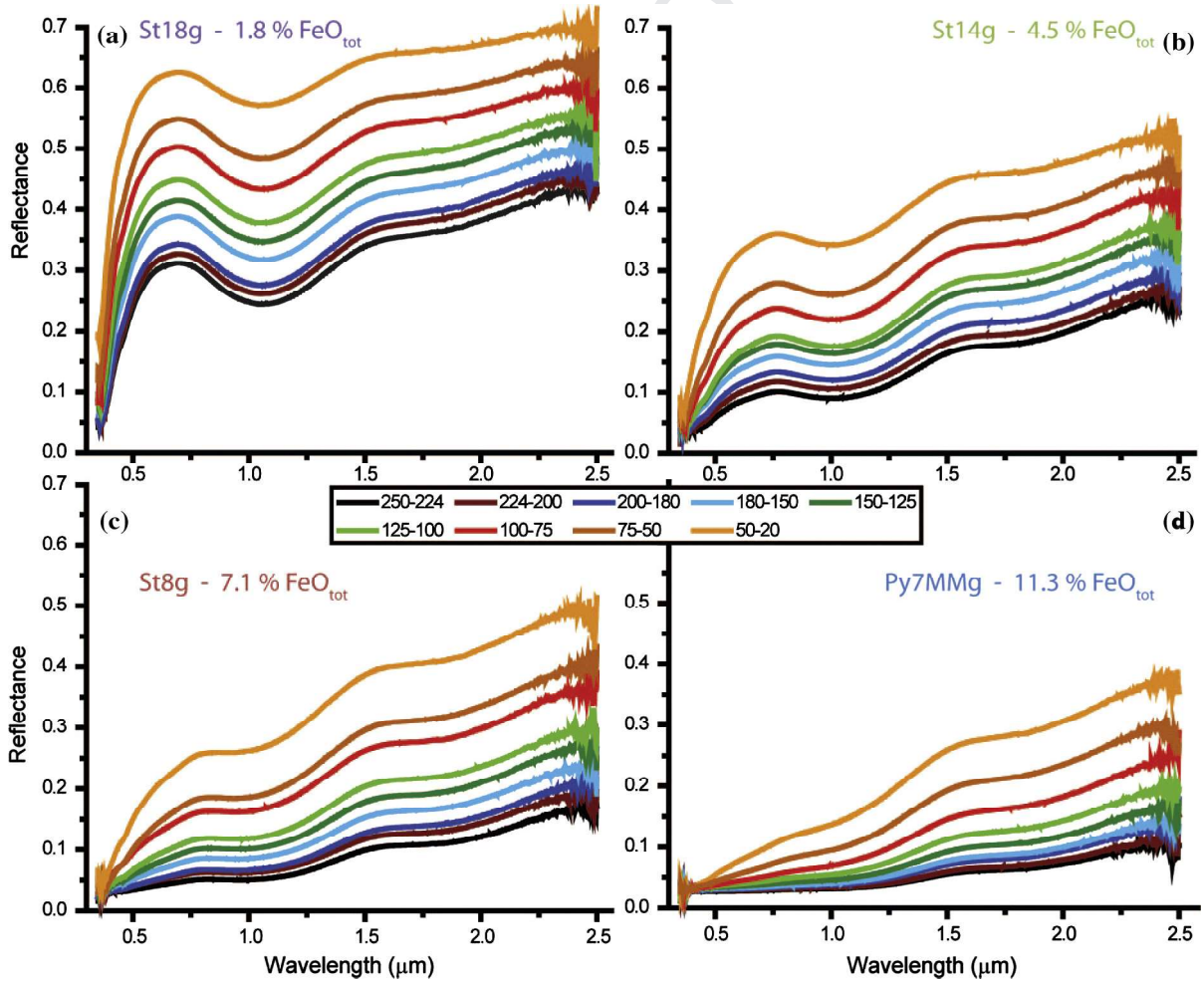

Fig. 5. Measured reflectance spectra of the four glasses at nine different particle sizes. (a) St18g (1.8 wt.% FeO_{tot}); (b) St14g (4.5 wt.% FeO_{tot}); (c) St8g (7.1 wt.% FeO_{tot}); (d) Py7MMg (11.3 wt.% FeO_{tot}). Particle size increases from high to low reflectance.

Please cite this article in press as: Carli, C., et al. Visible and Near-Infrared (VNIR) reflectance spectroscopy of glassy igneous material: Spectral variation, retrieving optical constants and particle sizes by Hapke model. Icarus (2015), http://dx.doi.org/10.1016/j.icarus.2015.10.032

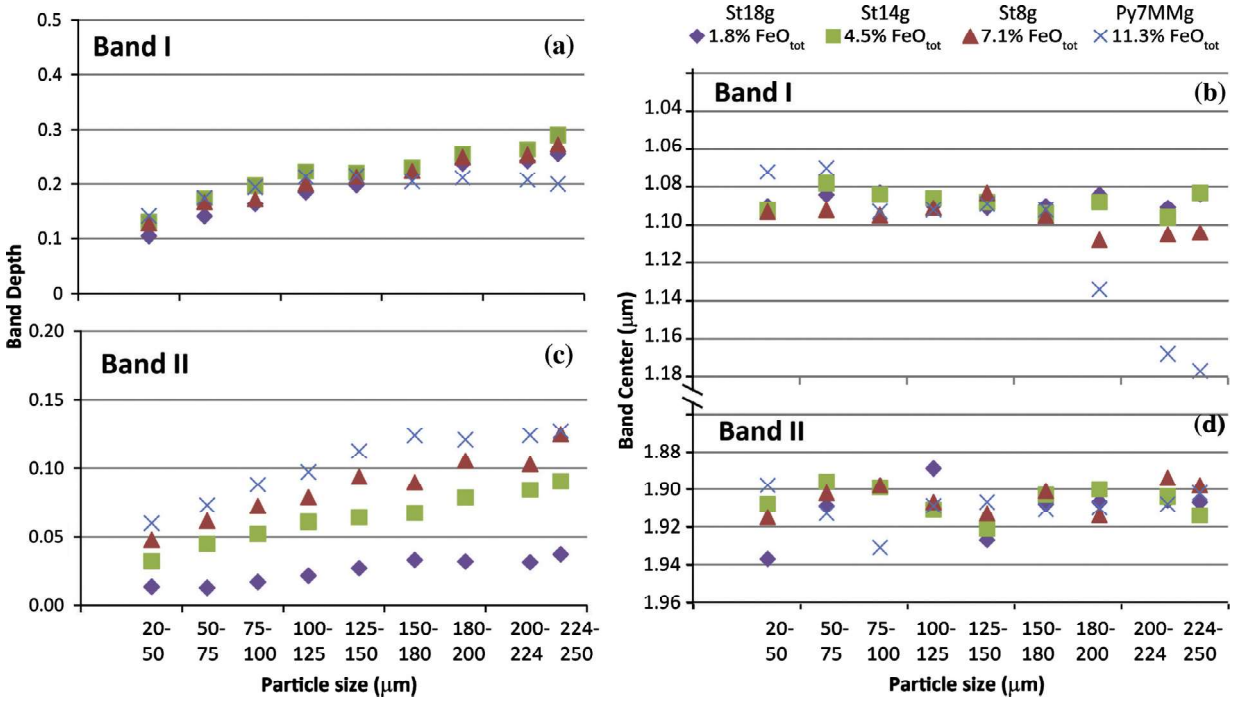

Fig. 6. Band depth and center vs. the particle size. (a and b) Band I parameters, it is evident the linear trend for the band depth (except for biggest sizes of iron richest sample Py7MMg), whereas no trend is present for the position of the band center (for biggest size of Py7MMg also the band center show an anomalous behavior). (c and d) Band II parameters show clear trend for the depth and no trend for the center, moreover band depth shows a clear variation with the iron content. To avoid the noise influence for the band at 1.9 μm we applied, for this spectral region, a smoothing function base on a Fast Fourier Transform algorithm using 50 data points, without significant effect on the diagnostic band center position. See text for more details.

has a low output and where the spectrometer sensitivity is decreased. All the spectra presented in Fig. 5 are used to retrieve the refractive indices, in this wavelength range. Using the approach described in Section 3.1 we find that after two iterations, there were no variations of n and k from the previous values. We considered these as our optical constants for each sample, and particle size. Because we assumed that the composition is not a function of particle size, we calculated a single mean, and associated standard deviation, from k-values obtained for each particle size and the resulting mean (ave1) is shown in Fig. 7 (white line), along with the standard deviation (gray vertical error bars). We show in Fig. 7 also the k-values for each sample and size. All the individual particle size k-values lie within or closer to one standard deviation, except for the two finest grain sizes. In particular, the k of finest size of iron-poor St18 g (panel a) shows a discrepancy at long wavelengths, whereas of 50–20s iron-rich Py7MMg (panel d) shows a high error in the visible. Because the finest particle sizes are not always within one standard deviation error we considered an alternative k averaging all particle sizes except the finest one (ave2). Fig. 8 shows that the 50–20 μm size only weakly influences the averages. The two average k-values (ave1, black, and, ave2, red lines) are almost superimposed, only the standard deviations are influenced by including (grey area) or not including (orange area) the finest size fraction.

4.3. Fitted particle size

We evaluate the ability of such average refractive indices being used to estimate particle size for an "unknown" measurement. As described in Section 3.2, we used the average (i.e. ave1) refractive indices to determine a particle size for each sample and size via a forward calculation of the Hapke model. Fig. 9 compares the particle sizes determined by fitting the spectra using to median sieve values. For all samples and sieve fractions the fitted particle sizes are within the sieve range (black lines), with only one exception, the coarsest size of St8g (7.1% FeO_{tot}). For the particle sizes between 50 and 200 μm the fitted values lie close to the median values (grey line). Fig. 10 shows that the relative error is generally $\leqslant$10% for 32 of the possible 36 cases. The exceptions are the finest size of St18g (1.8% FeO_{tot}) and St14g (4.5% FeO_{tot}), and the 75–50 and 250–224 μm sizes of St8g (7.1% FeO_{tot}). The relative error seems to have no correlation with the composition variation of our glasses.

4.4. Image analysis of particles

The measured particle size distribution of the two sieve separates, 250–224 and 50–20 μm, is shown in Figs. 11 and 12. We view this as a qualitative distribution of these materials. A more complete and accurate distribution would require sampling many more particles. While this can be achieved with commercial systems, these typically require grams of material that are unavailable for these samples. Alternatively, additional SEM imaging, and associated image analyses could be undertaken, but they are not readily automated making them very time consuming and are beyond the scope of the current study.

Nonetheless, the qualitative results provide some insight into the nature of the particles within these two sieve fractions. We have recast the numerical distributions (Fig. 11) into percentages of each particle size and the results are shown in Fig. 12a and b for the 250–224 μm size fraction. The percentage of very fine particles is 80–90%. However, as shown in Fig. 2, the fine grains only sparsely cover the surface of the larger particles. Moreover it is evident that several particles are bigger than the nominal sieve size range. Using the elliptical axes lengths suggests that the particles are not spherical. In fact the ratio major axis/minor axis is always >1, and occasionally approaches 3. This indicates that the particles

Please cite this article in press as: Carli, C., et al. Visible and Near-Infrared (VNIR) reflectance spectroscopy of glassy igneous material: Spectral variation, retrieving optical constants and particle sizes by Hapke model. Icarus (2015), http://dx.doi.org/10.1016/j.icarus.2015.10.032

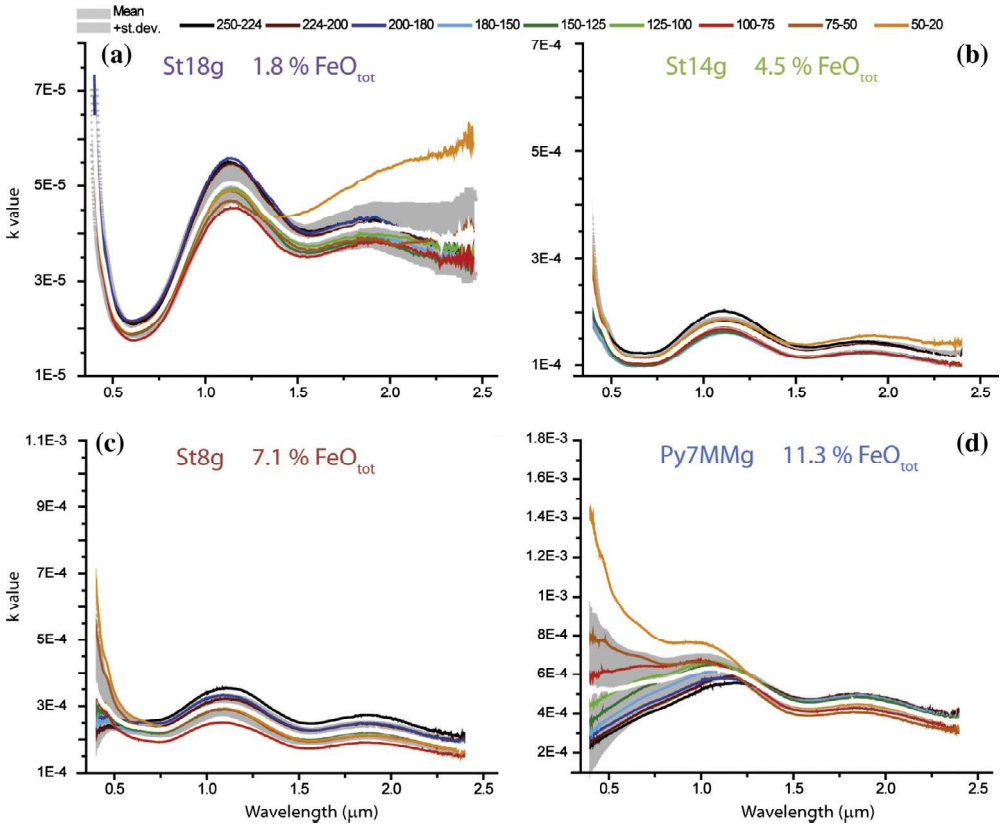

Fig. 7. Retrieved imaginary indices (k). The averaged values (considering all the relative k for each size) are in white with one standard deviation in grey. All the relative k for each size are reported. for each samples. (a) St18g; (b) St14g; (c) St8g; and (d) Py7MMg.

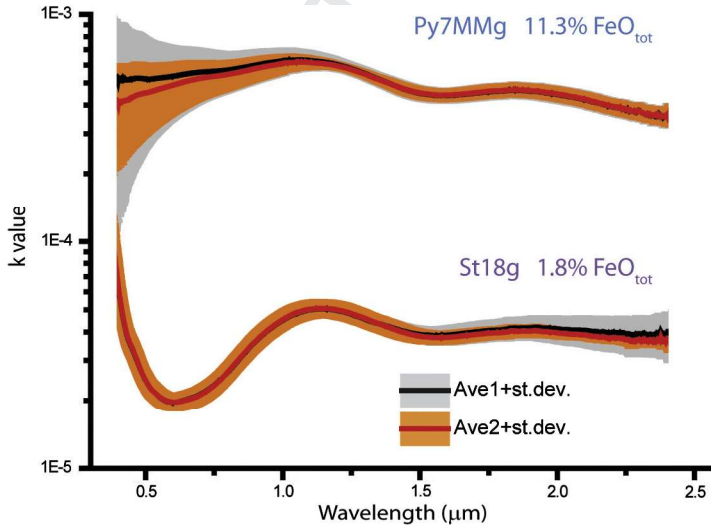

Fig. 8. k values for the two extreme composition considering the average of all the relative k (Ave1, black line, with grey area representative of the one standard deviation) or without 50–20 μm range (Ave2, red line, orange area is the one standard deviation). (For interpretation of the references to color in this figure legend, the reader is referred to the web version of this article.)

are irregular and elongated and during the sieving process the small grain axis could pass through the sieve.

Considering the 50–20 μm we can see that roughly 60–90% of particles are in the sieve size range (Fig. 12c). A notable exception is Py7MMg, the most Fe-rich, which has ~40% of the particles with diameters >50 μm size and the lowest percentage of fine particles. Conversely, sample St18g, the most Fe-poor, has the highest percentage of fine particles (>50%) and lowest percentage (4%) of large particles. While this is an intriguing relationship with Fe-content, the other two samples, St8g and St14g, fall in between these extremes, but apparently do not define a trend with Fe-content.

5. Discussion

In this work we have measured spectra of glasses with four different basic igneous compositions, dominated by varying amounts

Please cite this article in press as: Carli, C., et al. Visible and Near-Infrared (VNIR) reflectance spectroscopy of glassy igneous material: Spectral variation, retrieving optical constants and particle sizes by Hapke model. Icarus (2015), http://dx.doi.org/10.1016/j.icarus.2015.10.032

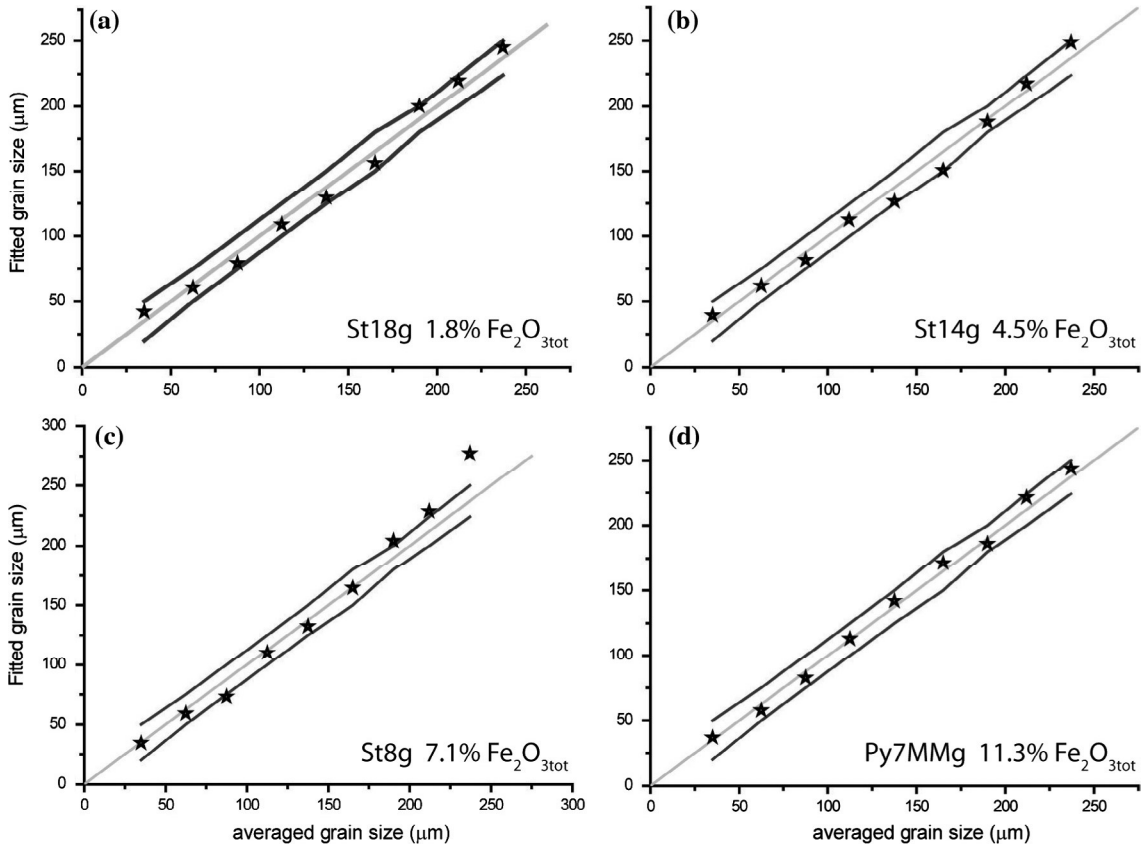

Fig. 9. Fitted size vs sieve sizes. Grey line show 1:1 ratio, black lines indicate the sieve limits. (a) St18g (1.8 wt.% FeO_{tot}); (b) St14g (4.5 wt.% FeO_{tot}); (c) St8g (7.1 wt.% FeO_{tot}); and (d) Py7MMg (11.3 wt.% FeO_{tot}).

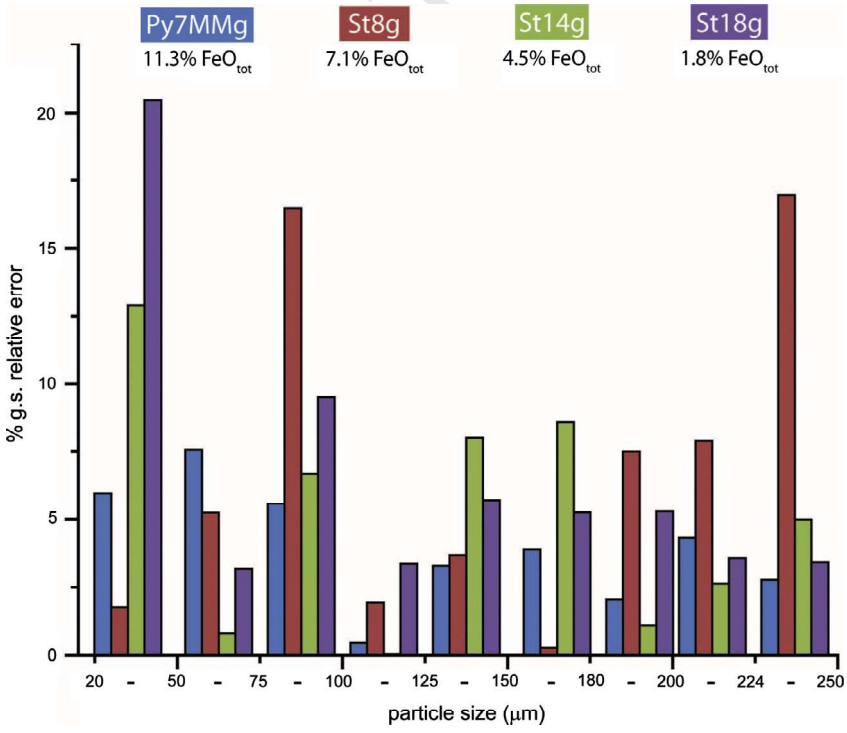

Fig. 10. Relative error for each fitted size with respect to the sieve average value.

of iron, and variable amount other major elements (like titanium, and calcium, alumina, see Table 1). The spectral variability between different samples is consistent with the different abundance of absorbing elements (i.e. iron) in the VNIR, despite the almost constant band center. In particular, increasing the amount of total iron results in the spectra becoming darker, flatter in the

Please cite this article in press as: Carli, C., et al. Visible and Near-Infrared (VNIR) reflectance spectroscopy of glassy igneous material: Spectral variation, retrieving optical constants and particle sizes by Hapke model. Icarus (2015), http://dx.doi.org/10.1016/j.icarus.2015.10.032

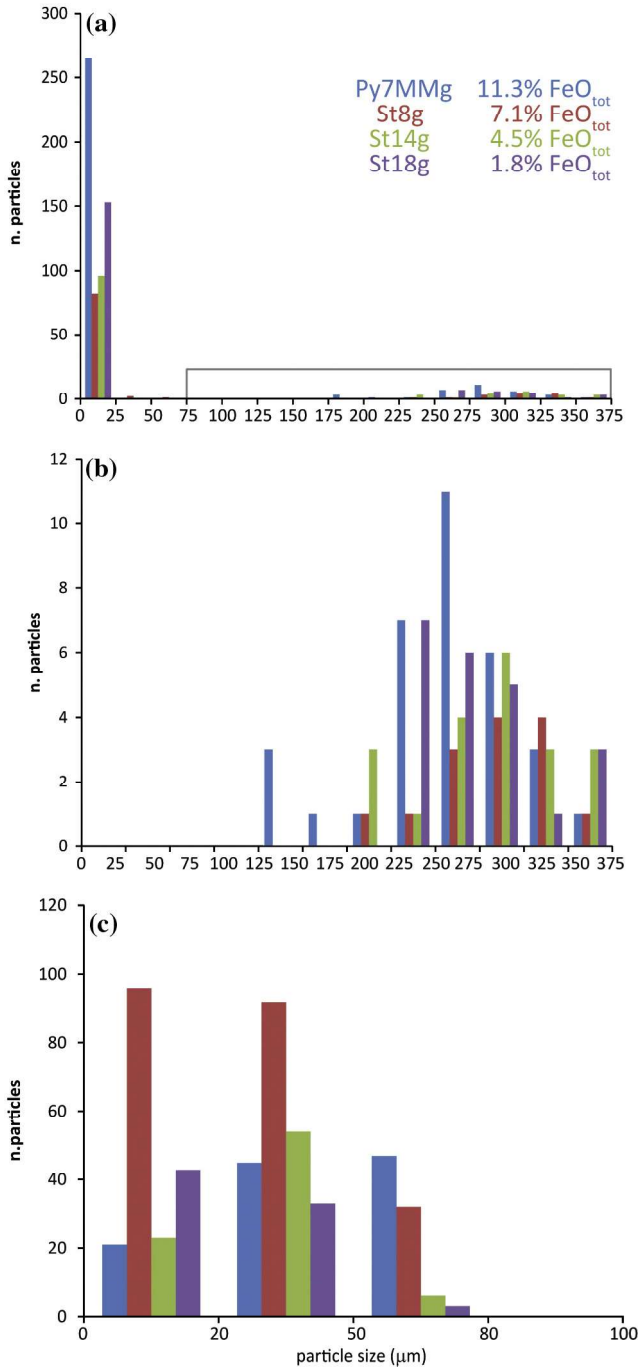

Fig. 11. Number of counted particles versus the re-calculated particle size. (a) All the particles for the 250–224 μm particle size (grey box indicate the range considered in image b). (b) Largest particle distribution, enlarged from box in panel a. (c) Particles counted for the 50–20 μm size range.

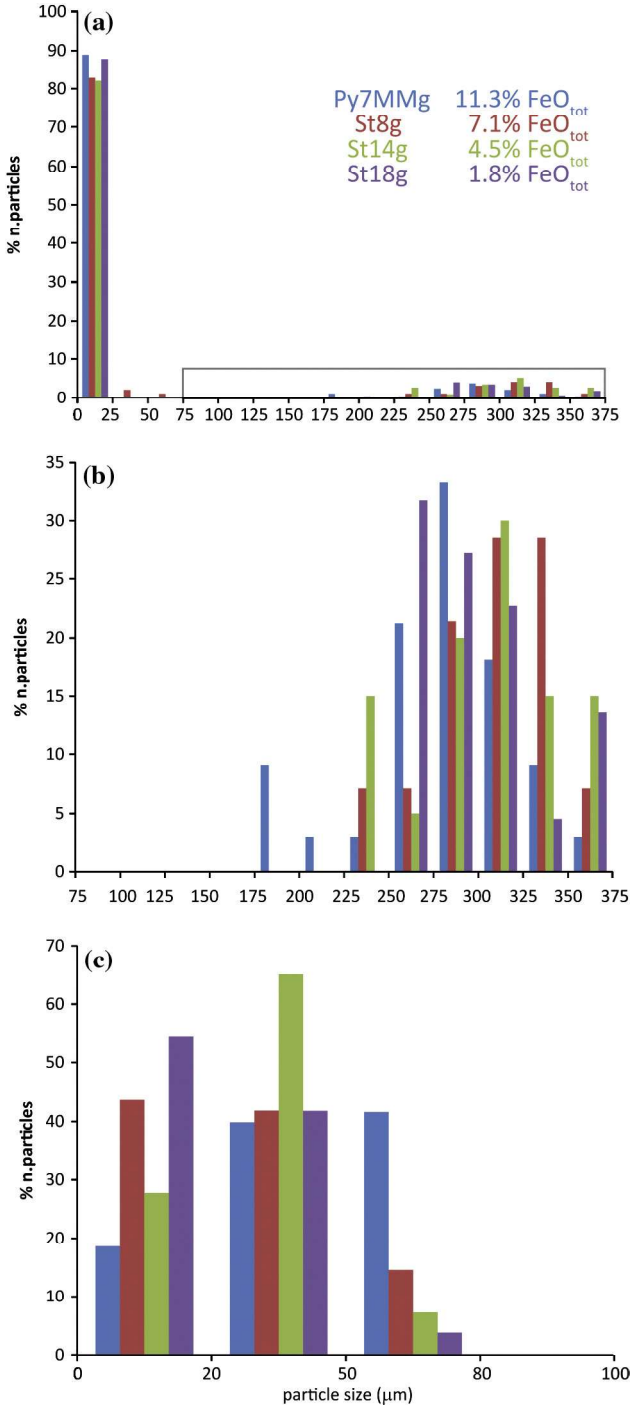

Fig. 12. Percent of counted particles versus the re-calculated particle size. (a) All the particles for the 250–224 μm particle size (grey box indicate the range considered in image b). (b) Largest particle distribution, box in panel a, recalculated to 100%. (c) Particles counted (as %) for the 50–20 μm size range.

visible, and redder towards the infrared, despite the Fe^{2+}/Fe^{3+} ratio being almost constant for all the samples (see Table 2). The increase of both Fe^{2+} and Fe^{3+} seems to affect the visible region, until the 0.8 μm shoulder of the CF absorption around 1.1 μm. Increasing the particle sizes also darkens the spectra, but maintains the spectral shape. Both the band depths vary linearly with the size but Band I depth is almost constant for the four composition.

We have retrieved the wavelength dependent real and imaginary parts of the refractive index via Hapke modeling (e.g. Hapke, 2012), and a sKK analysis. The *k*-values obtained for each of the 9 sieve size fractions are very close to falling within one standard deviation. So we calculated an average value for each sample (as done in several work in the literature, e.g. Lucey, 1998; Roush et al., 2007). We found that only the finest size fraction, specifically for the two extremes of Fe composition, have *k*-values falling outside of one standard deviation. This discrepancy is greatest at shorter wavelengths in the most Fe-rich sample, and at longer wavelengths in the most Fe-poor glass. Anyway these discrepancies do not significantly affect the average values (see Fig. 8).

The SEM image analyses, in addition, show how the finest particles (<20 μm, but generally within 1–5 μm) are abundant, even for the largest sieve size fraction. However, they sparsely populate

Please cite this article in press as: Carli, C., et al. Visible and Near-Infrared (VNIR) reflectance spectroscopy of glassy igneous material: Spectral variation, retrieving optical constants and particle sizes by Hapke model. Icarus (2015), http://dx.doi.org/10.1016/j.icarus.2015.10.032

the surfaces of the big particles. This is important because it is the cross section area that has the greatest impact in reflectance spectra and in our calculation. The reflectance measurements clearly show that the relative abundance of these finest particles do not significantly affect the reflectance. This implies that they do not significantly impact the retrieval of the complex refractive indices. Moreover we observe irregular shaped particles and typically <10%, by number, of the particles bigger than the nominal sieve size fraction, with the notable exception of the Fe-poor sample where it is 40%. In spite of this, we observe only a general monotonic behavior in the reflectance measurements as a function of sieve size fraction. This may be due to the random distribution of the particles in the sample holder. As a result we do not perceive the presence of these coarser grains introduce any residual error in the calculation of *k*-values. This perception is supported by the fact that, generally, all the *k*-values of individual particle size separates were within one standard deviation of the average. This suggests that interpreting the average sieve size as the diameter of the equivalent sphere is a reasonable approximation of the irregular particles randomly oriented.

Using the average refractive indices we applied a forward calculation of the Hapke model, to assess the ability to determine the particle size from the measured reflectance spectra. The result of this analysis showed that grain size associated with the best fit of the measured spectra always lies within the known sieve size ranges (Fig. 9). The relative errors (Fig. 10) associated with these analyses are always within a 10% of the sieve size mean values.

The capability to detect spectrally a surface glass component from remote sensing data is an important, largely under-studied, goal. In fact glassy material can be an important component of extrusive volcanism, and all the inner planets are mainly composed of effusive material, as well as a product of impact craters, and all the planetary bodies are characterized by these features. Here we have considered a range of compositions that span from plagioclase rich type, i.e. anorthositic, to more femic type, i.e. basaltic. We found that band center positions are almost unchanged despite the variable iron amount, and Band I is always in a different position compared to mafic minerals and iron bearing plagioclase, becoming diagnostic to the identification for an iron-bearing glass. The optical constants can be considered as analogs to glasses related to lunar Highland and basaltic compositions (e.g. lunar Maria, Martian lavas). In this study we considered glasses produced under terrestrial environmental conditions, and further discussion on the influence of oxygen fugacity on VNIR reflectance spectral characteristics is needed. Future efforts will investigate these samples as well as other compositions analogs to inner planetary bodies formed at different oxidizing conditions to strongly define the more appropriate optical constants for bodies having different oxidation conditions.

6. Conclusions

In this paper we have measured the visible and near-infrared spectral reflectance of synthetic glass samples, produced under terrestrial atmospheric conditions from rocks with different basic igneous compositions. We have seen that:

(1) Glass samples have the same composition of original bulk rock, in terms of major elements, Fe^{2+}/Fe^{3+} is almost constant for all the samples, the glasses density is lower of the corresponding original sample density.
(2) Reflectance spectra are always characterized by two absorptions with band centers close to 1.1 and 1.9 μm, with a small shift in position. With increasing particle size the spectra generally decrease in albedo. Increasing the iron content of the glass also produces a reduction in albedo, and a flattening in the visible region, with the 0.8 μm shoulder that almost disappearing. The spectral slope in the near infrared increases with the iron content. Moreover the band intensity varies linearly with the size for both the absorptions. But the 1.1 μm band depth shows very little difference varying composition. In contrast, the 1.9 μm depth increases with increasing iron content.
(3) The imaginary refractive indices were retrieved using the mean sieve value for each size of each glass sample. An average imaginary refractive index was calculated for each sample from the individual particle size results. For all samples, with a couple of exceptions, we found that the individual particle size imaginary refractive indices were all within one standard deviation of the mean value.
(4) Measured spectra were fit using the average complex refractive indices for each sample to model the particle size using a χ^2-criterion. Almost all the retrieved sizes are within the sieves range, and generally the relative errors do not exceed 10%.
(5) Despite the irregular and elongated shape of particles, as seen by SEM image analysis, spectral reflectance characteristics do not exhibit unusual trends, and as a result the associated retrieved complex refractive indices appear to be unaffected. Additionally, the fitted size results remain consistent with the nominal sieves range. This suggests that for powders with random orientation and narrow distribution ranges the averaged sieves size is a reasonable approximation of the effective cross section of the particles.

The reflectance spectra and the retrieved optical constants used in this paper are reported as online material.

7. Uncited references

Rasband and Image (1997). Q7

Acknowledgments

Rocks samples were kindly provided by Prof. M. Massironi (University of Padova) and Prof. O. Zeda (University of Parma). Glassy samples were produced at Volcanologist Laboratory with the help of Dr. A. Vona (RomaTre University). Authors thank Dr. D. Bersani and Dr. G. Serventi (University of Parma) for Brewster angles measurements.

XRF analyses and density measurements were performed at Geoscience Department, and Mössbauer data were collected at Biophysics and Medical Physics Unit, Department of Neuroscience, University of Parma. Reflectance spectra were carried out at Spectrocopic LABoratory at IAPS-INAF, Roma. We thank Dr. D. Blake of NASA Ames for access to the SEM for imaging and Dr. A. Brown (SETI) for his invaluable assistance in obtaining the SEM imaging. Moreover authors want to thanks Prof. E. Cloutis and an anonymous reviewer for their pertinent comments and suggestions that helped us to more clearly set the manuscript.

C. Carli wants to thanks T.L. Roush and Ames Research Center for hosting him during his month-long visit.

This work was financially supported by Agenzia Spaziale Italiana, SIMBIO-SYS project. Q8 Q9

Appendix A. Supplementary material

Supplementary data associated with this article can be found, in the online version, at http://dx.doi.org/10.1016/j.icarus.2015.10.032.

References

Abramoff, M.D., Magalhaes, P.J., Ram, S.J., 2004. Image processing with ImageJ. Biophoton. Int. 11 (7), 36–42.

Adams, J.B., McCord, T.B., 1971. Optical properties of mineral separates, glass, and anorthositic fragments from Apollo mare samples. In: Proceedings of the 2nd Lunar Science Conference, vol. 3, pp. 2183–2195.

Bell, P.M., Mao, H.K., Weeks, R.A., 1976. Optical spectra and electron paramagnetic resonance of lunar and synthetic glasses: a study of the effects of controlled atmosphere, composition, and temperature. In: Proceedings of the 7th Lunar Science Conference, pp. 2543–2559.

Burns, R.G., 1993. Mineralogical Applications of Crystal Field Theory. Cambridge University Press, Cambridge, 551 pp..

Carli, C., Sgavetti, M., 2011. Spectral characteristics of rocks: Effects of composition and texture and implications for the interpretation of planet surface compositions. Icarus 211, 1034–1048.

Carli, C. et al., 2014a. Spectral variability of plagioclase–mafic mixtures (2): Investigation of the optical constant and retrieved mineral abundance dependence on particle size distribution. Icarus 235, 207–219. http://dx.doi.org/10.1016/j.icarus.2014.03.022.

Carli, C., Serventi, G., Sgavetti, M., 2014b. VNIR spectral variability of the igneous stratified Stillwater Complex: A tool to map lunar highlands. Am. Min. 99, 1834–1848. http://dx.doi.org/10.2138/am-2014-4808.

Carli, C., Serventi, G., Sgavetti, M., 2015. VNIR spectral characteristics of terrestrial igneous effusive rocks: Mineralogical composition and the influence of texture. In: Platz, T., Massironi, M., Byrne, P.K., Hiesinger, H. (Eds.), Volcanism and Tectonism Across the Inner Solar System, vol. 401. Geological Society, London, Special Publications, pp. 139–158, doi:http://dx.doi.org/10.1144/SP401.19 (first published online June 17, 2014).

Church, B.N., Johnson, W.M., 1980. Calculation of the refractive index of silicate glasses from chemical composition. Geol. Soc. Am. Bull. 91, 619–625.

Clark, R.N., Roush, T.L., 1984. Reflectance spectroscopy: Quantitative analysis techniques for remote sensing applications. J. Geophys. Res. 89, 6329–6340.

Cloutis, E.A. et al., 1990. Reflectance spectra of glass-bearing mafic silicate mixtures and spectral deconvolution procedures. Icarus 86, 383–401.

Cruikshank, D.P. et al., 1997. The surfaces of Pluto and Charon. In: Stern, S.A., Tholen, D.J. (Eds.), Pluto and Charon. Univ. Arizona Press, Tucson, AZ, pp. 221–267.

Dorschner, J. et al., 1995. Steps toward interstellar silicate mineralogy: II. Study of Mg–Fe-silicate glasses of variable composition. Astron. Astrophys. 300, 503–520.

Dyar, M.D., Burns, R.G., 1981. Coordination chemistry of iron in glasses contributing to remote sensed spectra of the Moon. In: Proceedings of the Lunar Planetary Science, vol. 12B, pp. 695–702.

Fowle, F.E., 1921. Smithsonian Physical Tables. Springer.

Gillis-Davis, J.J., Lucey, P.G., Hammer, J.E., Wilcox, B.B., 2007. Syntheses and reflectance analyses of lunar red glass compositions: information to improve understanding of remotely sensed spectral data. In: Lunar Planetary Science XXXVIII, Abs. #1443.

Gillis-Davis, J.J., Lucey, P.G., Hammer, J.E., Denevi, B.B., 2008. Syntheses and reflectance analyses of lunar green glass compositions: information to improve understanding of remotely sensed spectral data. In: Lunar Planetary Science XXXXIX, Abs.#1535.

Hapke, B., 1981. Bidirectional reflectance spectroscopy 1. Theory. J. Geophys. Res. 86 (B4), 3039–3054.

Hapke, B., 1993. Theory of Reflectance and Emittance Spectroscopy. Topics in Remote Sensing, vol. 3. Cambridge University Press, Cambridge, UK.

Hapke, B., 2001. Space weathering from Mercury to the asteroid belt. J. Geophys. Res. 106, 10039–10073.

Hapke, B., 2008. Bidirectional reflectance spectroscopy. 6. Effects of porosity. Icarus 195, 918–926.

Hapke, B., 2012. Theory of Reflectance and Emittance Spectroscopy. Cambridge University Press, Cambridge, UK, 513 pp.

Jager, C. et al., 1994. Steps toward interstellar silicate mineralogy: I. Laboratory results of a silicate glass of mean cosmic composition. Astron. Astrophys. 292, 641–655.

Kaasalainen, S., 2003. Laboratory photometry of planetary regolith analogs. I. Effects of grain and packing properties on opposition effect. Astron. Astrophys. 409, 765–769.

Karamanov, A., Pelino, M., 1999. Evaluation of the degree of crystallisation in glass-ceramics by density measurements. J. Eur. Ceram. Soc. 19, 649–654.

Lagarec, K., Rancourt, D.G., 1998. Recoil: Mössbauer Spectral Analysis Software for Windows, Version 1.01998.

Lucey, P.G., 1998. Model near-infrared optical constants of olivine and pyroxene as a function of iron content. J. Geophys. Res. 103 (E1), 1703–1713.

Näränen, J. et al., 2004. Laboratory photometry of planetary regolith analogs. II. Surface roughness and extremes of packing density. Astron. Astrophys. 426, 1103–1109.

Pasquarè, G. et al., 2008. Very long Pahoehoe inflated basaltic lava flows in the payenia volcanic province (Mendoza and La Pampa, Argentina). Rev. Assoc. Geol. Arg. 63, 131–149.

Press, W.H. et al., 1992. Numerical Recipes in FORTRAN The Art of Scientific Computing, second ed. Cambridge University Press, New York, New York, 963 pp..

Rasband, W.S., xxxx. ImageJ. US National Institutes of Health, Bethesda, Maryland, USA, 1997–2014 <http://imagej.nih.gov/ij/>.

Roush, T.L., 1994. Charon: More than water ice? Icarus 108, 243–254.

Roush, T.L., 2003. Estimated optical constants of the Tagish Lake meteorite. Meteorit. Planet. Sci. 38, 419–426.

Roush, T.L., 2005. Near-infrared (0.67–4.7 μm) optical constants estimated for montmorillonite. Icarus 179, 259–264.

Roush, T.L. et al., 1990. Ice and minerals on Callisto: A reassessment of the reflectance spectra. Icarus 86, 355–382.

Roush, T.L. et al., 2007. Estimated optical constants of gypsum in the regions of weak absorptions: Application of scattering theories and comparisons to independent measurements. J. Geophys. Res.-Planets, 112, E10003, doi:http://dx.doi.org/10.1029/2007JE002920.

Roush, T.L. et al., 2014. Optical constants of Mars candidate materials used to model laboratory reflectance spectra of mixtures. Lunar Planetary Science XXXXV, Abs. # 1380.

Schneider, C.A., Rasband, W.S., Eliceiri, K.W., 2012. NIH Image to ImageJ: 25 years of image analysis. Nat. Meth. 9, 671–675.

Shepard, M.K., Helfenstein, P., 2011. A laboratory study of the bidirectional reflectance from particulate samples. Icarus 215, 526–533.

Tompkins, S., Pieters, C.M., 2010. Spectral characteristics of lunar impact melts and inferred mineralogy. Meteorit. Planet. Sci. 45, 1152–1169.

Warrel, J., Davidsson, B.J.R., 2010. A Hapke model implementation for compositional analysis of VNIR spectra of Mercury. Icarus 209, 164–178.

Wilcox, B.B., Lucey, P.G., Hawke, B.R., 2006. Radiative transfer modeling of compositions of lunar pyroclastic deposits. J. Geophys. Res. 111, E09001. http://dx.doi.org/10.1029/2006JE002686.

Please cite this article in press as: Carli, C., et al. Visible and Near-Infrared (VNIR) reflectance spectroscopy of glassy igneous material: Spectral variation, retrieving optical constants and particle sizes by Hapke model. Icarus (2015), http://dx.doi.org/10.1016/j.icarus.2015.10.032